

Probing entanglement dynamics and topological transitions on noisy intermediate-scale quantum computers

Huai-Chun Chang,^{1,2} Hsiu-Chuan Hsu,^{1,3,*} and Yu-Cheng Lin^{1,†}

¹*Graduate Institute of Applied Physics, National Chengchi University, Taipei 11605, Taiwan*

²*Physics Division, National Center for Theoretical Sciences, Taipei 10617, Taiwan*

³*Department of Computer Science, National Chengchi University, Taipei 11605, Taiwan*

(Dated: June 18, 2024)

We simulate quench dynamics of the Su-Schrieffer-Heeger (SSH) chain on the IBM quantum computers, calculating the Rényi entanglement entropy, the twist order parameter and the Berry phase. The latter two quantities can be deduced from a slow-twist operator defined in the Lieb-Schultz-Mattis theorem. The Rényi entropy is obtained using a recently developed randomized measurement scheme. The twist order parameter and the Berry phase are measured without the need for additional gates or ancilla qubits. We consider quench protocols in which a trivial initial state evolves dynamically in time under the topological SSH Hamiltonian in the fully dimerized limit (the flat-band limit). During these quenches, there are persistent and periodic oscillations in the time evolution of both entanglement entropy and twist order parameter. Through the implementation of error mitigation techniques using a global depolarizing ansatz and postselection, our simulations on the IBM devices yield results that closely match exact solutions.

I. INTRODUCTION

Nonequilibrium dynamics of quantum many-body systems is an active field of research both in condensed matter physics and quantum information science. Most of the efforts have focused on dynamics generated by a quantum quench, i.e. a sudden change of parameters in the Hamiltonian, because it poses important fundamental questions that can be investigated in controlled experiments [1]. Among experimental systems, ultracold atoms have proven to be the ideal arena to realize systems' Hamiltonians and simulate quantum dynamics using the inherent quantum mechanical properties [2, 3]. Recently, cold-atom systems have been further developed to programmable devices [4] that embody Richard Feynman's proposal for an analog quantum computer [5].

Here we focus on quantum quench dynamics implemented by another type of quantum computing approach, namely digital quantum computing, or called gate-based quantum computing. In the digital approach, quantum simulations are carried out by sequences of quantum gates applied to a small number of physical qubits, mimicking classical computations. One key advantage of digital quantum computing is the versatility and universality it offers, as any operation can be expressed as a finite set of gates [6]. However, gate errors and noise often limit the depth of a quantum circuit where layers of the required quantum gates are built. Moreover, one may need to use the Trotter decomposition [7] to approximately decompose the unitary time evolution into a product of one or two-qubit gates while simulating the quantum dynamics of a many-body system in the digital approach, which generates additional systematic errors. To obtain the best possible results from today's noisy intermediate-scale quantum (NISQ) devices, numerous techniques for error correction [8, 9], error mitigation [10] and optimization strategies [11] have been

developed in the past few years.

Several studies have demonstrated the potential of digital quantum computing for quantum many-body simulations [12]. In particular, various entanglement properties, such as entanglement spectra [13], symmetry-resolved entropies [14], the second-order Rényi entropy [15, 16], for many-body ground states and dynamical states have been actively explored on current quantum computers. There is also an increasing interest in probing topological properties with NISQ devices; recent works include measuring string order parameters crossing symmetry protected topological phase transitions [17], simulating chiral topological dynamics [18], and probing fractional quantum Hall states [19].

In this work, we simulate quench dynamics of the Su-Schrieffer-Heeger (SSH) chain [20], a paradigmatic model for topological insulators, on IBM-Q devices. Considerable efforts have been made over the past years to elucidate topological dynamical phenomena in quantum quenches between different topological phases in the SSH model, predominantly focusing on the Bloch state in momentum space [21–25]. Here we focus on observables in real space, for up to 12 qubits. We quantify the entanglement using the second-order Rényi entanglement entropy and probe topological properties using the twist operator appearing in the Lieb-Schultz-Mattis theorem [26, 27]. We consider a special case where the dynamics of entanglement and topology exhibits persistent and periodic oscillations. This simulation can be executed without Trotter errors, enabling us to evaluate the ability of NISQ devices to simulate quantum many-body dynamics through comparisons with exact solutions.

The paper is organized as follows: In Sec. II, we define the model and the quench protocols considered in our simulations; we summarize some known properties of the quench dynamics. In Sec. III, we describe our simulation setups on the IBM-Q devices and present our simulation results, focusing on the Rényi entanglement entropy and twist order parameters. We conclude in Sec. IV with a summary and discussion.

* hcjhsu@nccu.edu.tw

† yc.lin@nccu.edu.tw

II. THE MODEL AND QUENCH PROTOCOLS

We consider the spin-1/2 XX chain of $L = 2N$ spins with alternating bond strength, defined by the Hamiltonian:

$$\begin{aligned}
H_{\text{XX}} = & \sum_{j=1}^N J (\sigma_{2j-1}^x \sigma_{2j}^x + \sigma_{2j-1}^y \sigma_{2j}^y) \\
& + \sum_{j=1}^{N-1} J' (\sigma_{2j}^x \sigma_{2j+1}^x + \sigma_{2j}^y \sigma_{2j+1}^y) \\
& + J'_{2N} (\sigma_{2N}^x \sigma_1^x + \sigma_{2N}^y \sigma_1^y)
\end{aligned} \quad (1)$$

where σ_j^α ($\alpha = x, y$) is the α -component of the Pauli matrix at site j ; J and J' are coupling constants on odd and even links, respectively. The coupling constant on the link $j = 2N$ is $J'_{2N} = J'$ for periodic boundary conditions (PBC), and is zero ($J'_{2N} = 0$) for open boundary conditions (OBC). The system consists of two sublattices A and B , where sublattice A contains all even sites and sublattice B contains all odd sites.

The XX spin chain is effectively a non-interacting fermion model [26]. Using the Jordan–Wigner transformation, the dimerized XX model defined above can be mapped to the SSH model, which is a half-filled chain of free fermions with alternating hopping described as

$$\begin{aligned}
H_{\text{SSH}} = & \sum_{m=1}^{N-1} (2J a_m^\dagger b_m + 2J' b_m^\dagger a_{m+1} + \text{h.c.}) \\
& + 2J a_N^\dagger b_N - (-1)^N 2J' b_N^\dagger a_1 + \text{h.c.},
\end{aligned} \quad (2)$$

where m indexes N unit cells that are pairs of two sites, one on sublattice A and one on B . The operators a_m^\dagger (b_m^\dagger) creates a spinless fermion at the A (B)-sublattice site in the m th unit cell, and N is the the number of fermions. The constants $2J$ and $2J'$ are regarded as the intracell and intercell hopping amplitudes, respectively. The boundary term is affected by the parity of the number of fermions [26]; depending on evenness or oddness of N , the boundary conditions of the fermionic chain are antiperiodic or periodic.

We consider the case with PBC and use the Fourier transform of the form:

$$\begin{pmatrix} a_m \\ b_m \end{pmatrix} = \frac{1}{\sqrt{N}} \sum_k e^{ikm} \begin{pmatrix} a_k \\ b_k \end{pmatrix}. \quad (3)$$

The Hamiltonian in momentum space can be written as

$$H_{\text{SSH}} = \sum_k \Psi_k^\dagger H_k \Psi_k, \quad (4)$$

with $\Psi_k^\dagger = (a_k^\dagger, b_k^\dagger)$ and a single-particle Bloch Hamiltonian $H_k = \mathbf{d}_k \cdot \boldsymbol{\sigma}$, where $\boldsymbol{\sigma}$ is the Pauli matrix and the vector $\mathbf{d}_k = (d_k^x, d_k^y, d_k^z)$ is given by

$$\mathbf{d}_k = (2J + 2J' \cos(k), 2J' \sin(k), 0). \quad (5)$$

The eigenvalues of the two-level Bloch Hamiltonian are given by

$$E_\pm = \pm |\mathbf{d}_k| = \pm 2\sqrt{J^2 + 2JJ' \cos(k) + J'^2}, \quad (6)$$

and the corresponding eigenvectors are

$$|\psi_\pm\rangle = \frac{1}{\sqrt{2}} \begin{pmatrix} \pm e^{-i\phi(k)} \\ 1 \end{pmatrix} \quad (7)$$

with $\phi(k) = \tan^{-1}(d_k^y/d_k^x)$. The dispersion relation in Eq.(6) describes a band structure with a gap $\Delta_E = 4|J - J'|$ at $k = \pm\pi$, as long as $J \neq J'$. In the fully dimerized cases ($J > 0, J' = 0$, or vice versa $J = 0, J' > 0$), the band structure becomes flat, i.e. independent of the wavenumber k . In this flat-band limit, there is also no difference between the periodic and antiperiodic boundary conditions. The topological properties of the system are encoded in the closed curve that the vector \mathbf{d}_k traces out as k changes from 0 to 2π . For $J < J'$, the curve encloses the origin $\mathbf{d}_k = \mathbf{0}$ and the system is in the topological phase; for $J > J'$, the origin is completely outside the closed curve, corresponding to a trivial phase. At the critical point $J = J'$ where the band gap closes, the curve passes through the origin. The number of times that the closed curve goes around the origin is referred to as the winding number ν , defining a topological invariant. Other useful tools to characterize topological properties include entanglement measures [21, 22, 28] and the Berry phase [29–32].

A transition between two distinct topological phases can occur without crossing a critical point, but rather by breaking chiral symmetry. This phenomenon arises when the vector \mathbf{d}_k is no longer confined to the (d_k^x, d_k^y) -plane and instead possesses a finite d_k^z component. Such a scenario is observed in nonequilibrium dynamics following a sudden quench of certain Hamiltonian parameters [21, 22], even when d_k^z is absent in both pre-quench and post-quench Hamiltonians. Here we focus on quenches with the flat-band Hamiltonian with $(J, J') = (0, 1)$. Two types of initial (pre-quench) states are considered: (i) a classical Néel state described by

$$|\psi_N\rangle = \bigotimes_{j=1}^N |1_{2j-1} 0_{2j}\rangle, \quad (8)$$

in terms of the standard basis of z spin components: $\sigma^z |0\rangle = |0\rangle$, $\sigma^z |1\rangle = -|1\rangle$, and (ii) a fully dimerized state described by a product of intracell singlets written as

$$|\psi_S\rangle = \bigotimes_{j=1}^N \frac{1}{\sqrt{2}} (|0_{2j-1} 1_{2j}\rangle - |1_{2j-1} 0_{2j}\rangle), \quad (9)$$

which is equivalent to the ground state of the trivial flat-band Hamiltonian with $(J, J') = (1, 0)$. For a quench from $|\psi_N\rangle$, the post-quench state will reach a winding number $\nu = 1$ at times $t_N = (n - \frac{1}{2})\frac{\pi}{4}$ with $n \in \mathbb{Z}^+$; for a quench from $|\psi_S\rangle$, the post-quench state will have a winding number $\nu = 2$ at $t_S = (n - \frac{1}{2})\frac{\pi}{2}$ [21, 22]. Below we denote by t_N^* and t_S^* those time points at which a finite winding number occurs. In real space, the periodic generation of the winding number manifests itself in the dynamics of intercell entanglement formation [33]. For the initial $|\psi_N\rangle$ state, the post-quench state consists of a set of nearest neighbor intercell entangled states

at $t = t_N^*$; For the initial $|\psi_S\rangle$ state, the post-quench state develops entangled states connecting A and B sublattices in two next-nearest-neighbor cells (i.e. extended to three lattice spacings) at times $t = t_S^*$.

A. Entanglement entropy

The formation of intercell entanglement in the post-quench states and their dynamics can be probed by entanglement entropy (EE). Each maximally entangled state that connects a block of contiguous sites with the rest of the system contributes one unit to the block EE (both Rényi and von Neumann entropies). In our settings, the post-quench state at times $t_{N(S)}^*$ evolves to a product of maximally entangled states, the EE of a segment embedded in the chain is then just the number of entangled states that connect sites inside to sites outside the segment. For a closed chain divided into two subsystems, the maximum EE for the state $|\psi_N(t)\rangle$ at t_N^* is 2, while it is 4 for the state $|\psi_S(t)\rangle$ at t_S^* . To observe the time evolution of entanglement, we consider the second-order Rényi EE, defined as

$$S = -\log_2 \text{Tr}[\rho_I^2], \quad (10)$$

where ρ_I is the reduced density matrix for a subsystem (denoted by I) in the bipartite system. Using the correlation matrix approach proposed in Ref. [34], we can obtain the Rényi EE via

$$S = -\sum_i \log_2 [1 - 2\xi_i(1 - \xi_i)], \quad (11)$$

where ξ_i is an eigenvalue of the correlation matrix. We consider a closed chain of length $L = 4\ell$ with an integer $\ell \geq 1$ and a symmetric bipartition such that each subsystem contains ℓ complete unit cells. For a quench from $|\psi_N\rangle$, the dynamical Rényi EE of a half chain is

$$S^{0 \rightarrow 1}(t) = -2 \log_2 [1 - \sin^2(2|\mathbf{d}_k|t)/2]. \quad (12)$$

where the superscript $0 \rightarrow 1$ indicates the change in the winding number under the quench. For a quench from the fully dimerized state $|\psi_S\rangle$ in which a transition to $\nu = 2$ occurs, the half-chain Rényi EE for a chain with $\ell > 1$ evolves as

$$S^{0 \rightarrow 2}(t) = -4 \log_2 [1 - \sin^2(|\mathbf{d}_k|t)/2]. \quad (13)$$

We note that $S^{0 \rightarrow 2}(t) = 2S^{0 \rightarrow 1}(t/2)$ [see Fig. 1(a)]. For a short closed chain of length $L = 4$ with only two unit cells, the dynamical Rényi EE is reduced to $S^{0 \rightarrow 1}(t)$.

B. Twist operator

A unitary operator, called the twist operator, defined via the spin operator S^z ($S^z = \sigma^z/2$ for spin-1/2) as

$$U_z = \exp\left(i \frac{2\pi}{L} \sum_{j=1}^L j S_j^z\right), \quad (14)$$

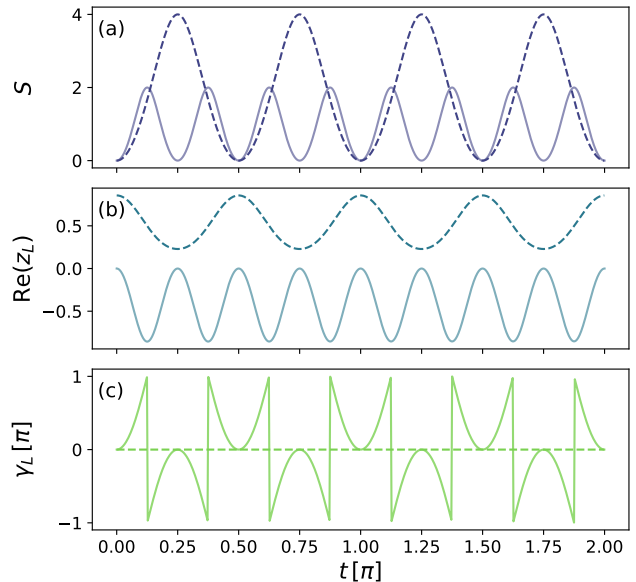


FIG. 1. Exact data for quenches from a Néel state $|\psi_N\rangle$ (solid lines) and from a fully dimerized state $|\psi_S\rangle$ (dashed lines), driven by the flat-band Hamiltonian with $(J = 0, J' = 1)$ and periodic boundary conditions. The panels from top to bottom show the evolution of (a) the Rényi entanglement entropy with a symmetric bipartition, (b) the twist order parameter for $L = 16$ and, (c) the Berry phase for $L = 16$.

for a spin chain of length L , is a useful tool to characterize various topology properties. This unitary operator was first introduced in the Lieb-Schultz-Mattis (LSM) theorem [26], which states that the amplitude, dubbed as the twist order parameter, given by

$$z_L^{(q)} = \langle \psi | U_z^q | \psi \rangle \quad (15)$$

in terms of the ground state of the XXZ spin chain can be seen as an indicator of a gapped or gapless excitation spectrum, depending on whether $z_L^{(q)}$ is nonvanishing or zero in the thermodynamic limit $L \rightarrow \infty$. Furthermore, the twist order parameter was generalized to higher spin cases and is capable of detecting the patterns of valence-bond-solid-like dimerization in the state $|\psi\rangle$ [27], even for random and inhomogeneous systems [35]. The real part of z_L is negative/positive for a dimerized state with strong links connecting adjacent sites $(j, j+1)$ with even/odd j (i.e. intercell/intracell links).

Here we apply the twist operator to the dynamical states in our quench protocols. As shown in Fig. 1(b) for $L = 16$, the twist order parameter oscillates in the region $\text{Re}[z_L] \leq 0$ for a quench from the Néel state $|\psi_N\rangle$, while it oscillates in the region $\text{Re}[z_L] > 0$ for a quench from the initial state $|\psi_S\rangle$. The oscillation of $\text{Re}[z_L]$ for the case of $|\psi_N\rangle$ indicates that the strongest dimerization occurs at t_N^* when the maximum entanglement forming between nearest neighboring cells; for the case of $|\psi_S\rangle$, the system starts from a fully dimerized state with intracell links and returns to this strongest dimerization after a period of $\pi/2$.

For the free-fermion model we consider here, the twist operator can be used to define localization length and electric polarization [36, 37]. Following Refs. [36, 38], we consider the unitary operator in terms of the particle number operator, $n_j = S_j^z + 1/2$, at each site,

$$U_n = \exp\left(i\frac{2\pi}{L}\sum_{j=1}^L jn_j\right). \quad (16)$$

Similar to the twist order parameter z_L , the ground-state expectation value

$$z_N^{(q)} = \langle \psi | U_n^q | \psi \rangle, \quad (17)$$

is an order parameter that distinguishes an insulating phase and a conducting phase at rational filling $n = p/q$ (where p/q is an irreducible fraction) [39], depending on whether $z_N^{(q)} \neq 0$ or $z_N^{(q)} = 0$ in the limit of $L \rightarrow \infty$ [37]. The argument of $z_N^{(q)}$ defines the center of mass of the particles, which is related to the Berry phase γ_L via [36, 39]

$$\gamma_L = \text{Im} \ln[z_N^{(q)}]. \quad (18)$$

We apply U_n^q with $q = 2$ for our dynamical states at half filling ($n = 1/2$). As shown in Fig. 1(c) The Berry phase for $|\psi_N(t)\rangle$ jumps between $-\pi$ and π at $t = t_N^*$, indicating a quantized dynamical Chern number $C = \pm 1$; this result agrees with previous studies based on the single-particle Hamiltonian in momentum space [25]. On the other hand, the Berry phase for $|\psi_S(t)\rangle$ remains zero for all t , reflecting that the dynamical state has inversion symmetry.

III. SIMULATIONS

In this section we present the relevant setups for our simulations on the IBM quantum computers, and show simulation results for dynamical entanglement entropy and the time-dependent twist order parameter.

A. Time evolution

The default state on the IBM devices is a tensor product of $|0\rangle$ and the computational basis is also composed by the tensor product of the eigenstates of σ^z . We set up the initial states $|\psi_N\rangle$ and $|\psi_S\rangle$ for our quench protocol using the Pauli gate \mathbf{X} , the Hadamard gate \mathbf{H} and the controlled-not (CNOT) gate \mathbf{C}_X , as shown in Fig. 2, where a two-spin singlet state is realized by a set of quantum gates $(\mathbf{X} \otimes \mathbf{X})(\mathbf{H} \otimes \mathbf{I})(\mathbf{C}_X)$.

For the post-quench Hamiltonian, the fully dimerized XX chain with $(J, J') = (0, 1)$, that we consider here, the quantum circuit for the time evolution operator $U(t) = \exp(-iHt)$ with an arbitrary time duration t can be constructed without the use of the Trotter decomposition. The time evolution operator can be split into

$$U(t) = \bigotimes_j U_{2j}(t) \quad (19)$$

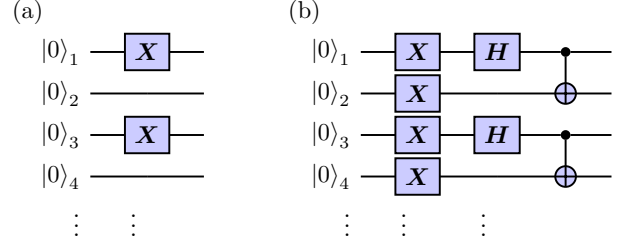


FIG. 2. Quantum gates for preparing the initial states: (a) the Néel state $|\psi_N\rangle$ and (b) the fully dimerized state with intracell singlets $|\psi_S\rangle$.

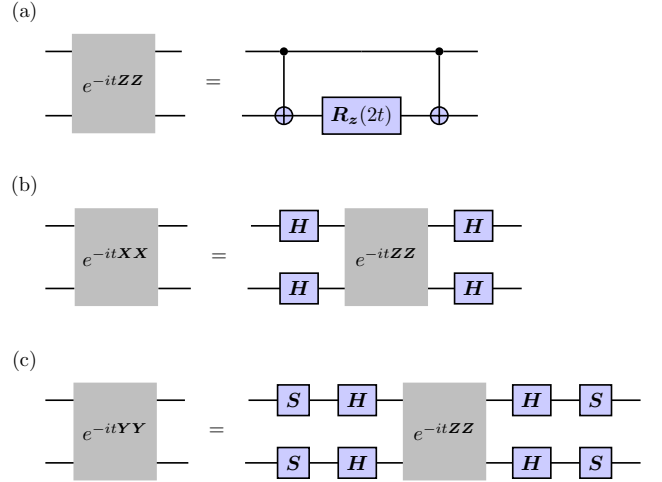


FIG. 3. Quantum circuits to implement the time-evolution operators $U^{zz}(t)$, $U^{xx}(t)$ and $U^{yy}(t)$.

with

$$U_{2j}(t) = \exp[-it(\sigma_{2j}^x \sigma_{2j+1}^x + \sigma_{2j}^y \sigma_{2j+1}^y)] \quad (20)$$

$$= \exp(-it\sigma_{2j}^x \sigma_{2j+1}^x) \exp(-it\sigma_{2j}^y \sigma_{2j+1}^y),$$

where the commutator identity $[\sigma_j^x \sigma_{j'}^x, \sigma_j^y \sigma_{j'}^y] = 0$ is applied. The quantum circuits required for the time evolution are then the gates to implement the operators $U^{xx}(t) = e^{-it\mathbf{X}\mathbf{X}}$ and $U^{yy}(t) = e^{-it\mathbf{Y}\mathbf{Y}}$, which can be transformed from the time evolution operator of an Ising spin pair $U^{zz}(t) = e^{-it\mathbf{Z}\mathbf{Z}}$. The circuit for the operator $U^{zz}(t)$ is composed of a rotation gate $\mathbf{R}_z(2t)$ and two \mathbf{C}_X gates, as shown in Fig. 3 (a). We can convert the operator $U^{zz}(t)$ into $U^{xx}(t)$ using Hadamard gates via $\mathbf{H}\mathbf{Z}\mathbf{H} = \mathbf{X}$. Similarly, we implement $U^{yy}(t)$ by wrapping the time-evolution operator $U^{zz}(t)$ with Hadamard gates and \mathbf{S} -gates on each qubit, where \mathbf{S} is a phase shift gate that rotates a $\pi/2$ radian about the z -axis, inducing $\mathbf{S}\mathbf{X}\mathbf{S} = \mathbf{Y}$. The circuits for $U^{xx}(t)$ and $U^{yy}(t)$ are shown in Fig. 3 (b) and Fig. 3 (c), respectively.

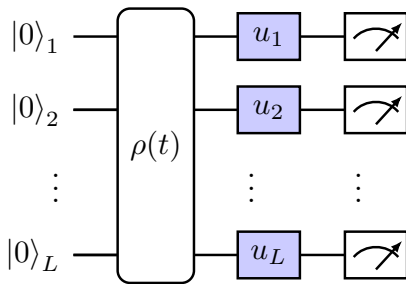


FIG. 4. Randomized measurements implemented on an L -qubit state $\rho(t)$ using single-qubit Haar random unitaries $\{u_i\}$ followed by a measurement in the computational basis

B. The Rényi entanglement entropy

The key ingredient of the second-order Rényi entropy is the purity $\text{Tr}[\rho^2]$ of a given (reduced) density matrix. A recently developed measurement protocol employing statistical correlations of locally randomized measurements [40–42] enables us to measure the purity with an adequate accuracy on current noisy quantum devices via classical postprocessing. This measurement procedure for our simulation of the Rényi entanglement entropy is as follows: (i) Generate a post-quench state, $\rho(t)$, of L qubits at time t ; (ii) Draw N_U sets random unitaries of the form $U = u_1 \otimes \cdots \otimes u_L$, where the u_i are single-qubit Haar random unitaries sampled independently from the circular ensemble [41, 43]; (iii) Apply each set of U to the state $\rho(t)$ and measure the probabilities $P(s_I)$ of obtaining computational basis states $|s_I\rangle = |s_1, \dots, s_{N_I}\rangle$ for the considered subsystem I of N_I qubits. The purity $\text{Tr}[\rho_I^2]$ for the reduced density matrix is then estimated using

$$\text{Tr}[\rho_I^2] = 2^{N_I} \sum_{s_I, s'_I} (-2)^{-D[s_I, s'_I]} \overline{P(s_I)P(s'_I)}, \quad (21)$$

where $D[s_I, s'_I] \equiv |\{j \in I | s_j \neq s'_j\}|$ is the Hamming distance between $|s_I\rangle$ and $|s'_I\rangle$, and $\overline{\cdots}$ denotes the ensemble average over the N_U sets of random unitaries. From $\text{Tr}[\rho_I^2]$, we obtain the Rényi EE (see Eq. (10)). This procedure is implemented for each instant of time that we consider to obtain the time-dependent Rényi EE $S(t)$. In our simulations $N_U = 100$ sets of random unitaries and $N_M = 2^{12}$ measurements per circuit were used to collect one data point, unless otherwise stated. We completed the measurements and the postprocessing through a parallel automation program [44] that we have developed for our simulations to efficiently calculate the entanglement entropy.

Fig. 5 shows the simulation results for short chains with $L = 4$ from the IBM devices, compared with exact data. The $L = 4$ system is a special case in which the half-chain entanglement entropies starting from both initial states $|\psi_N\rangle$ and $|\psi_S\rangle$ have the same form of time dependence. Here we observe a clear qualitative agreement between the numerical data from the IBM devices and exact solutions. In particular, the period of the oscillations and the EE values around the peaks

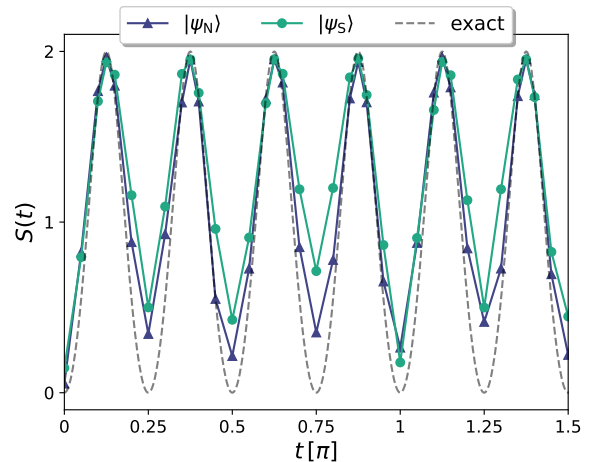


FIG. 5. Results for the half-chain entanglement entropy for a chain with $L = 4$ and PBC after quenches from the initial states $|\psi_N\rangle$ and $|\psi_S\rangle$, simulated on the IBM device *ibm_mumbai*.

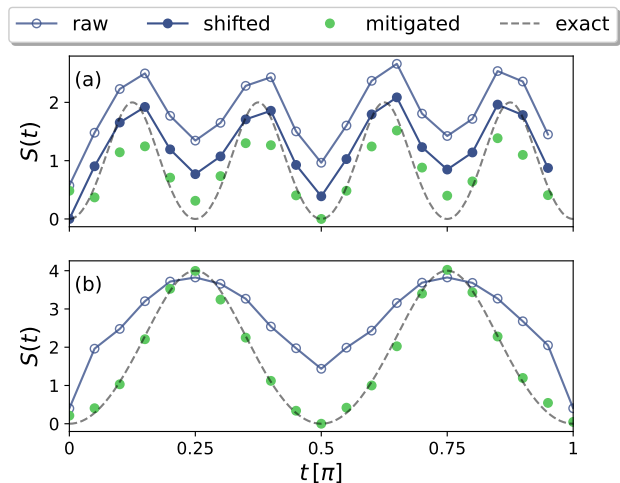


FIG. 6. Results for the half-chain entanglement entropy for a chain with $L = 8$ and PBC after quenches from the initial states $|\psi_N\rangle$ (a) and $|\psi_S\rangle$ (b), simulated on the IBM device *ibm_montreal*. The results for $|\psi_S\rangle$ after applying error mitigation using the global depolarizing ansatz show an excellent match with the exact solution.

are accurately produced in the raw data from the IBM device.

For longer chains, there is however a serious decline in the accuracy of the simulation results, as shown in Fig. 6 for $L = 8$. For the initial state $|\psi_N\rangle$, there is an entropy shift when compared to the exact solution. This offset, possibly some inherent error in the device, can be partially eliminated by aligning the entropy at $t = 0$ with the exact value $S(t = 0) = 0$. We note that the shift mitigation approach has also been applied in previous studies [45]. To eliminate the deviations beyond the constant shift, we apply a simple error mitigation strategy using the global depolarizing noise ansatz, along the lines of Ref. [15]. We assume that the entire quantum state of L qubits

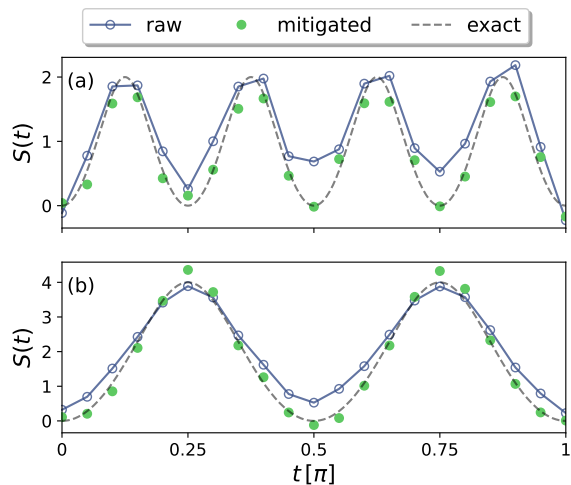


FIG. 7. Results for the entanglement entropy of four bulk qubits in an open chain with $L = 8$ after quenches from the initial states $|\psi_N\rangle$ and $|\psi_S\rangle$, simulated on *ibm.auckland*. The error-mitigated data are adjusted to align the average value of the valley minima to zero.

under the noise is

$$\rho = (1 - p_{\text{tot}})\rho_{\text{exact}} + \frac{p_{\text{tot}}}{2L}\mathbb{1}, \quad (22)$$

where p_{tot} is the total probabilistic error rate and ρ_{exact} is the exact density matrix without noise. With the assumption in Eq. (22), we have the relation between the purities for the noisy density matrix obtained from randomized measurements and for the exact density matrix:

$$\text{Tr}[\rho_I^2] = (1 - p_{\text{tot}})^2 \text{Tr}[\rho_{I,\text{exact}}^2] + \frac{p_{\text{tot}}(1 - p_{\text{tot}})}{2^{N_I-1}} + \frac{p_{\text{tot}}^2}{2^{N_I}}, \quad (23)$$

where I denotes a subsystem of N_I qubits. The error rate p_{tot} can be extracted from $\text{Tr}[\rho^2]$ when the full density matrix for a pure state is considered since $\text{Tr}[\rho_{\text{exact}}^2] = 1$. We have determined p_{tot} for each time step to carry out the error mitigation for the time-dependent data. In addition, the mitigated data in Fig. 6 are adjusted to align the minimum to zero to correct negative entropies in the minima. The results for $|\psi_S\rangle$ after applying error mitigation clearly show an excellent match with the exact data, while the mitigated results for $|\psi_N\rangle$ with global depolarizing ansatz are merely passable.

The deviation from the exact solutions can have more than one source. For example, the accuracy of the estimated purity by randomized measurements depends crucially on the number of random unitaries and the number of measurements per random unitary [41], as implied in Eq. (21). However, the primary source of error for our case may stem from the PBC imposed on the model, which requires connectivity between the first and last qubits via ancilla qubits and additional gates, thereby leading to higher error rates. For example, the circuit depth for the simulations of the chains with PBC is 40 (45) for the initial state $|\psi_N\rangle$ ($|\psi_S\rangle$), while the depth is reduced to 15 (19) when open chains with OBC are considered. We can indeed reproduce the results for $L = 8$ with higher accuracy by using a segment of bulk qubits (from the 3rd to the 6th qubit)

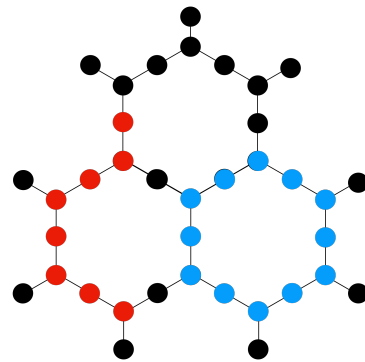


FIG. 8. A schematic plot of the heavy-hexagon lattice, widely adopted in the IBM quantum processors. Each circle represents a physical qubit. The blue circles form a ring layout and the red circles form a line layout that are selected in our simulations for a 8-qubit chain and a 12-qubit chain, respectively.

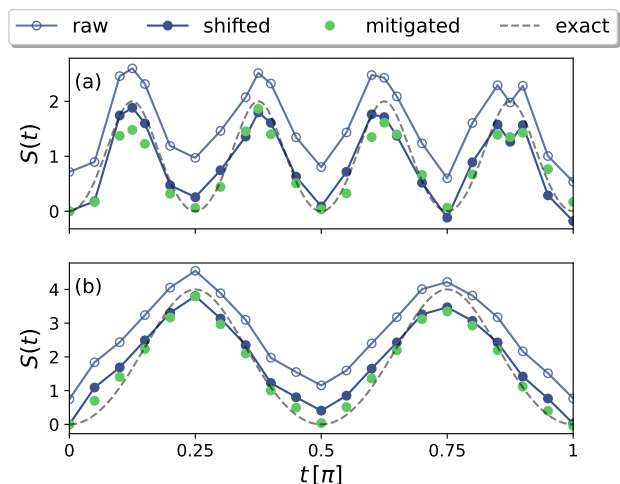


FIG. 9. Results for the half-chain entanglement entropy for a chain with $L = 12$ and PBC after quenches from the initial states $|\psi_N\rangle$ (a) and $|\psi_S\rangle$ (b). The simulations were carried out on *ibmq.mumbai*. For $L = 12$, we carried out $N_M = 2^{14}$ measurements per circuit to reduce statistical error in the calculation of the estimator in Eq. (21).

in an open chain as the subsystem considered for the EE. The results for the open chain displayed in Fig. 7 largely agree quantitatively with the exact data, even without applying error mitigation. After applying the global depolarizing error mitigation, the overall shape of the EE as a function of time, in particular around the entropy valleys, is corrected. However, we need to apply a constant shift to align the entropy at $t = 0$ (the minimum entropy) to zero.

In addition to the 4- and 8-qubit systems, we also utilize the IBM heavy-hexagon lattice to simulate a 12-qubit chain with PBC that forms a ring in the hexagonal arrangement (see Fig. 8). The circuit depth required in our simulations for the 12-qubit system in this ring layout is the same as for the 8-qubit chain with OBC, namely 15 layers for the initial state $|\psi_N\rangle$ and 19 layers for $|\psi_S\rangle$. Although the number of qubits is increased to 12, the results for the dynamical entanglement

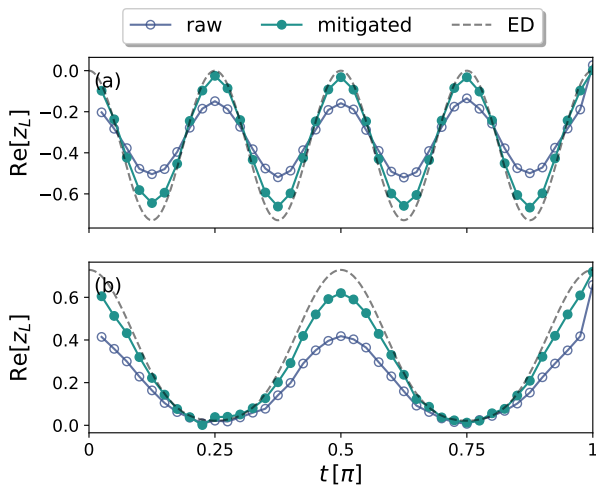


FIG. 10. Results, obtained from *ibm_auckland*, for the twist order parameter for a chain with $L = 8$ and PBC after quenches from the initial states $|\psi_N\rangle$ (a) and $|\psi_S\rangle$ (b).

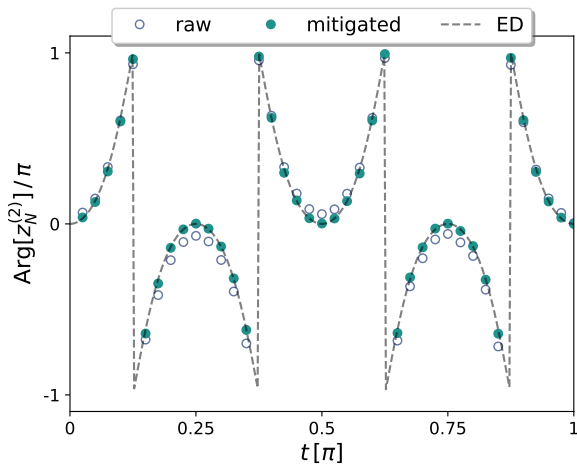


FIG. 11. The dynamical Berry phase for a chain with $L = 8$ and PBC after a quench from the initial states $|\psi_N\rangle$, simulated on *ibm_auckland*.

entropy, shown in Fig. 9, match well with the exact solutions through the simple shift mitigation, and can be further improved with the global depolarizing error mitigation.

C. The twist operator

The twist operator defined in Eq. (14) is equivalent to a product of \mathbf{R}_z rotation operators: $\otimes_{j=1}^L \mathbf{R}_z(\theta_j)$ with $\theta_j = -2\pi j/L$ for the angle of rotation on the j th-qubit. In practice, we can circumvent the accumulated errors resulting from the series of rotation operators by directly measuring $\otimes_{j=1}^L \mathbf{Z}$ for each instant of time, a straightforward process in the computational basis. Given a set of measured bitstrings $\{\mathbf{s} : \mathbf{s} = s_1 s_2 \dots s_L \text{ with } s_j = 0 \text{ or } 1\}$ with occurring probabilities $P(\mathbf{s})$, the twist order parameter z_L (defined in Eq. (15)) is

then obtained via postprocessing using

$$z_L = \sum_{\mathbf{s}} \exp \left[i \frac{\pi}{L} \sum_{j=1}^L j(1 - 2s_j) \right] P(\mathbf{s}). \quad (24)$$

The unmitigated data for z_L in Fig. 10, both for the initial states $|\psi_N\rangle$ and $|\psi_S\rangle$, display oscillations with periods identical to those of the exact diagonalization (ED) results, but have considerably smaller amplitudes. We have applied a simple postselection method by only considering bitstrings with an equal number of '0's and '1's, in accordance with particle number (magnetization) conservation requirements. We find an increase in amplitudes for the data after postselecting; in particular, the results for quenches starting from the Néel state $|\psi_N\rangle$ have shown good quantitative agreement with ED results.

Now we turn to the results for the Berry phase defined in Eq. (18) with $q = 2$. Similar to z_L , the amplitude $z_N^{(q)}$ is obtained by

$$z_N^{(2)} = \sum_{\mathbf{s}} \exp \left[i \frac{4\pi}{L} \sum_{j=1}^L j(1 - s_j) \right] P(\mathbf{s}). \quad (25)$$

for a set of bitstrings $\{\mathbf{s}\}$ with occurring probabilities $P(\mathbf{s})$. The Berry phase is then the argument of this complex amplitude: $\gamma_L = \text{Arg}[z_N^{(2)}]$. Here we only consider the case for the initial state $|\psi_N\rangle$ since the case for $|\psi_S\rangle$ has zero Berry phase in the quench dynamics. We have used the same bitstrings from the IBM device for z_L and the same postselected bitstrings to calculate the amplitude $z_N^{(2)}$. In comparison to the twist order parameter $\text{Re}[z_L]$, the Berry phase, as the argument of $z_N^{(2)}$, appears to be more robust against noise. As shown in Fig. 11, the Berry phase obtained from the IBM Q device after error mitigation is in perfect agreement with exact diagonalization results.

IV. SUMMARY AND DISCUSSION

We have simulated quantum quenches in the SSH chain on NISQ devices provided by IBM. We considered particularly simple quench protocols in which the time evolution is governed by the topological SSH Hamiltonian in the fully dimerized limit. This time evolution can be implemented without the use of the Trotter decomposition. Our simulations on the IBM-Q devices demonstrated periodic oscillations in entanglement dynamics after a quench from a topologically trivial state, reflecting periodic transitions between two phases with different topological structures. We have also detected such dynamical topology using the twist order parameter and the Berry phase, which can be measured on a quantum device without the need for additional gates. Through some error mitigation techniques, we were able to deduce time-dependent data that match exact solutions for up to 12 qubits.

The layout of qubits significantly impacts the accuracy of our simulation results. Specifically, simulating a 8-qubit chain

with PBC requires more than twice as many circuit layers compared to a 8-qubit chain with OBC, leading to increased noise. On the other hand, the IBM heavy-hex lattice, which consists of 12-qubit rings with nearest-neighbor couplings, provides an ideal platform for our simulations of 12-qubit chains with PBC using shallow circuits.

To mitigate noise on NISQ computers, we applied postselection based on symmetry conservation to twist order parameters and the Berry phase. The mitigated results agree very well with the exact solutions. However, this simple mitigation method cannot be applied to the entanglement entropy because the randomized measurement protocol requires the application of random unitary gates that break symmetry constraint. In some cases, the overall structure of the unmitigated time-dependent entanglement entropy is correct except for a constant deviation from the exact solution, which can be corrected by applying a constant shift to align the entropy at $t = 0$ to zero (the theoretical value). In some cases, the unmitigated entanglement entropy as a function of time is misshapen and the largest amplitude of the oscillation is smaller than the theoretical value; we were able to correct the shape

and the amplitudes through a global depolarizing error mitigation method [15]. However, a constant shift to align the minimum entropy to zero is often required after applying the global depolarizing error mitigation. By combining global depolarizing error mitigation and shift mitigation, we were able to achieve mitigated results that are in excellent agreement with the exact solutions.

The LSM twist operator applied in our simulations can formulate various quantities and concepts fundamental to quantum many-body physics, such as order parameters to characterize gapped phases [27, 46], Berry phases [36], polarization [36] and localization length [37]. Recently, the applications of the LSM twist operator have also been generalized to open quantum systems [47, 48]. The twist operator is diagonal in the computational basis on quantum computers. This property allows us to calculate its related quantities on classical computers by processing the bit-strings and their corresponding probabilities from quantum device measurements, without incurring additional overhead in quantum hardware. The method makes many interesting applications of the twist operator amenable to simulations on NISQ devices.

-
- [1] A. Mitra, Quantum Quench Dynamics, Annual Review of Condensed Matter Physics **9**, 245 (2018).
- [2] T. Kinoshita, T. Wenger and D. S. Weiss, A quantum Newton's cradle, Nature **440**, 900 (2006).
- [3] M. Gring, et al., Relaxation and Prethermalization in an Isolated Quantum System, Science **337**, 1318 (2012).
- [4] K. Wintersperger, F. Dommert, T. Ehmer, A. Hoursanov, J. Klepsch, W. Mauere, et al., Neutral Atom Quantum Computing Hardware: Performance and End-User Perspective, EPJ Quantum Technology **10**, 32 (2023).
- [5] R. P. Feynman, Simulating physics with computers, Int. J. Theor. Phys. **21**, 467 (1982).
- [6] M. A. Nielsen and I. L. Chuang, Quantum Computation and Quantum Information: 10th Anniversary Edition, 10th ed. (Cambridge University Press, USA, 2011).
- [7] H. F. Trotter, On the Product of Semi-Groups of Operators, Proc. Am. Math. Soc. **10**, 545 (1959).
- [8] E. H. Chen, T. J. Yoder, Y. Kim, N. Sundaresan, S. Srinivasan, M. Li, A. D. Córcoles, A. W. Cross, and M. Takita, Calibrated Decoders for Experimental Quantum Error Correction, Phys. Rev. Lett. **128**, 110504 (2022).
- [9] Sundaresan, N., Yoder, T.J., Kim, Y. et al. Demonstrating multi-round subsystem quantum error correction using matching and maximum likelihood decoders. Nat Commun **14**, 2852 (2023).
- [10] Z. Cai, R. Babbush, S. C. Benjamin, S. Endo, W. J. Huggins, Y. Li, J. R. McClean, and T. E. O'Brien, Quantum error mitigation, Rev. Mod. Phys. **95**, 045005 (2023).
- [11] E. Kökcü, D. Camps, L. B. Ofeltie, J. K. Freericks, W. A. de Jong, R. Van Beeumen, and A. F. Kemper, Algebraic compression of quantum circuits for Hamiltonian evolution, Phys. Rev. A **105**, 032420 (2022).
- [12] B. Fauseweh, Quantum many-body simulations on digital quantum computers: State-of-the-art and future challenges, Nature Communications **15**, 2123 (2024).
- [13] K. Choo, C. W. von Keyserlingk, N. Regnault, and T. Neupert, Measurement of the entanglement spectrum of a symmetry-protected topological state using the ibm quantum computer, Phys. Rev. Lett. **121**, 086808 (2018).
- [14] D. Azses, R. Haenel, Y. Naveh, R. Raussendorf, E. Sela, and E. G. Dalla Torre, Identification of symmetry-protected topological states on noisy quantum computers, Phys. Rev. Lett. **125**, 120502 (2020).
- [15] J. Vovrosh, K. E. Khosla, S. Greenaway, C. Self, M. S. Kim, and J. Knolle, Simple mitigation of global depolarizing errors in quantum simulations, Phys. Rev. E **104**, 035309 (2021).
- [16] N. Mueller, J. A. Carolan, A. Connelly, Z. Davoudi, E. F. Dumitrescu, and K. Yeter-Aydeniz, Quantum computation of dynamical quantum phase transitions and entanglement tomography in a lattice gauge theory, PRX Quantum **4**, 030323 (2023).
- [17] A. Smith, B. Jobst, A. G. Green, and F. Pollmann, Crossing a topological phase transition with a quantum computer, Phys. Rev. Research **4**, L022020 (2022).
- [18] J. M. Koh, T. Tai, and C. H. Lee, Simulation of Interaction-Induced Chiral Topological Dynamics on a Digital Quantum Computer, Phys. Rev. Lett. **129**, 140502 (2022).
- [19] A. Kirmani, K. Bull, C.-Y. Hou, V. Saravanan, S. M. Saeed, Z. Papić, A. Rahmani, and P. Ghaemi, Probing Geometric Excitations of Fractional Quantum Hall States on Quantum Computers, Phys. Rev. Lett. **129**, 056801 (2022).
- [20] W. P. Su, J. R. Schrieffer, and A. J. Heeger, Solitons in Polyacetylene, Phys. Rev. Lett. **42**, 1698 (1979).
- [21] P.-Y. Chang, Topology and entanglement in quench dynamics, Phys. Rev. B **97**, 224304 (2018).
- [22] Z. Gong and M. Ueda, Topological entanglement-spectrum crossing in quench dynamics, Phys. Rev. Lett. **121**, 250601 (2018).
- [23] C. Yang, L. Li, and S. Chen, Dynamical topological invariant after a quantum quench, Phys. Rev. B **97**, 060304 (2018).
- [24] X.-Y. Guo, C. Yang, Y. Zeng, Y. Peng, H.-K. Li, H. Deng, Y.-R. Jin, S. Chen, D. Zheng, and H. Fan, Observation of a dynamical quantum phase transition by a superconducting qubit simulation, Phys. Rev. Applied **11**, 044080 (2019).
- [25] H.-C. Hsu, P.-M. Chiu, and P.-Y. Chang, Disorder-induced topology in quench dynamics, Phys. Rev. Research **3**, 033242

- (2021).
- [26] E. Lieb, T. Schultz, and D. Mattis, Two Soluble Models of an Antiferromagnetic Chain, *Annals of Physics* **16**, 407 (1961).
- [27] M. Nakamura and S. Todo, Order Parameter to Characterize Valence-Bond-Solid States in Quantum Spin Chains, *Phys. Rev. Lett.* **89**, 077204 (2002).
- [28] J. Sirker, M. Maiti, N. P. Konstantinidis, and N. Sedlmayr, Boundary fidelity and entanglement in the symmetry protected topological phase of the SSH model, *J. Stat. Mech.* P10032 (2014).
- [29] M. V. Berry, Quantal phase factors accompanying adiabatic changes, *Proc. R. Soc. Lond. A* **392** 45 (1984).
- [30] J. Zak, Berry's phase for energy bands in solids, *Phys. Rev. Lett.* **62**, 2747 (1989).
- [31] M. Atala, M. Aidelsburger, J. T. Barreiro, D. Abanin, T. Kitagawa, E. Demler, and I. Bloch, Direct measurement of the Zak phase in topological bloch bands, *Nature Physics* **9**, 795 (2013).
- [32] C. G. Velasco and B. Paredes, Realizing and detecting a topological insulator in the AIII symmetry class, *Phys. Rev. Lett.* **119**, 115301 (2017).
- [33] I. Mondragon-Shem, T. L. Hughes, J. Song, and E. Prodan, Topological Criticality in the Chiral-Symmetric AIII Class at Strong Disorder, *Phys. Rev. Lett.* **113**, 046802 (2014).
- [34] I. Peschel, Calculation of reduced density matrices from correlation functions, *J. Phys. A: Math. Gen.* **36**, L205 (2003).
- [35] Y.-T. Lin, S.-F. Liu, P. Chen, Y.-C. Lin, Random singlets and permutation symmetry in the disordered spin-2 Heisenberg chain: A tensor network renormalization group study, *Phys. Rev. Research* **5**, 043249 (2023).
- [36] R. Resta, Quantum-Mechanical Position Operator in Extended Systems, *Phys. Rev. Lett.* **80**, 1800 (1998).
- [37] R. Resta and S. Sorella, Electron Localization in the Insulating State, *Phys. Rev. Lett.* **82**, 370 (1999).
- [38] R. Kobayashi, Y. O. Nakagawa, Y. Fukusumi, and M. Oshikawa, Scaling of the polarization amplitude in quantum many-body systems in one dimension, *Phys. Rev. B* **97**, 165133 (2018).
- [39] A. A. Aligia and G. Ortiz, Quantum Mechanical Position Operator and Localization in Extended Systems, *Phys. Rev. Lett.* **82**, 2560 (1999).
- [40] T. Brydges, A. Elben, P. Jurcevic, B. Vermersch, C. Maier, B. P. Lanyon, P. Zoller, R. Blatt, and C. F. Roos, Probing Rényi entanglement entropy via randomized measurements, *Science* **364**, 260 (2019).
- [41] A. Elben, B. Vermersch, C. F. Roos, and P. Zoller, Statistical correlations between locally randomized measurements: A toolbox for probing entanglement in many-body quantum states, *Phys. Rev. A* **99**, 052323 (2019).
- [42] A. Elben, S. T. Flammia, H.-Y. Huang, R. Kueng, B. Vermersch, and P. Zoller, The randomized measurement toolbox, *Nature Reviews Physics* **5**, 9 (2023).
- [43] F. Mezzadri, How to generate random matrices from the classical compact groups, *Notices AMS* **54**, 592 (2007).
- [44] The program is available at: http://github.com/harui2019/qurry_preview.
- [45] J. Vovrosh and J. Knolle, Confinement and entanglement dynamics on a digital quantum computer, *Scientific Reports* **11**, 11577 (2021).
- [46] T. Hirano, H. Katsura, and Y. Hatsugai, Topological classification of gapped spin chains: Quantized Berry phase as a local order parameter, *Phys. Rev. B* **77**, 094431 (2008).
- [47] K. Kawabata, R. Sohal, and S. Ryu, Lieb-Schultz-Mattis theorem in open quantum systems, *Phys. Rev. Lett.* **132**, 070402 (2024).
- [48] Y.-N. Zhou, X. Li, H. Zhai, C. Li, and Y. Gu, Reviving the Lieb-Schultz-Mattis theorem in open quantum systems, *arXiv:2310.01475* (2023).

ACKNOWLEDGMENTS

The authors acknowledge support from the IBM Q Hub at National Taiwan University, the National Science and Technology Council (NSTC) and the National Center for Theoretical Sciences (NCTS) in Taiwan. This work was supported under Grants No. NSTC 111-2119-M-007-009 and 112-2119-M-007-008.